

# Extreme low-latitude TEC enhancement and GPS Scintillation at dawn

Sebastijan Mrak<sup>1,1</sup>, Joshua L. Semeter<sup>1,1</sup>, Yukitoshi (Toshi) Nishimura<sup>1,1</sup>, and Anthea Coster<sup>2,2</sup>

<sup>1</sup>Boston University

<sup>2</sup>MIT Haystack Observatory

November 30, 2022

## Abstract

We report on an extreme ionospheric plasma density enhancement and Global Positioning System (GPS) scintillation at dawn, observed within the expanding equatorial ionization anomaly (EIA). The total electron content (TEC) in central America reached 50~TECu at sunrise, the value almost twice as high as the normal afternoon peak. The enhanced EIA expanded poleward and westward from just below 20\$^\circ\$ magnetic latitude (MLAT) to beyond 30\$^\circ\$ MLAT at sunrise. The chief ramification of the enhanced EIA was strong GPS scintillation which was observed poleward of 30\$^\circ\$ northern MLAT and lasted until 8:00 local time. In total, the scintillation lasted for \$\sim\$5~hours at latitudes north of 20\$^\circ\$ MLAT in central America.

# Extreme low-latitude TEC enhancement and GPS Scintillation at dawn

Sebastijan Mrak<sup>1</sup>, Joshua Semeter<sup>1</sup>, Yukitoshi Nishimura<sup>1</sup>, and Anthea J.  
Coster<sup>2</sup>

<sup>1</sup>Department of Electrical and Computer Engineering and Center for Space Physics, Boston University,  
Boston, MA, USA

<sup>2</sup>Haystack Observatory, Massachusetts Institute of Technology, Westford, MA, USA

## Key Points:

- Observations show expansion of equatorial ionization anomaly (EIA) beyond 35° magnetic latitude at a pre-dawn time.
- Total electron content of the EIA's northern crest in central America exceeded 50 TECu at sunrise.
- The EIA was accompanied by equatorial plasma bubbles, causing severe GPS scintillations lasting for five hours around sunrise.

---

Corresponding author: Sebastijan Mrak, [smrak@bu.edu](mailto:smrak@bu.edu)

## Abstract

We report on an extreme ionospheric plasma density enhancement and Global Positioning System (GPS) scintillation at dawn, observed within the expanding equatorial ionization anomaly (EIA). The total electron content (TEC) in central America reached 50 TECu at sunrise, the value almost twice as high as the normal afternoon peak. The enhanced EIA expanded poleward and westward from just below 20° magnetic latitude (MLAT) to beyond 30° MLAT at sunrise. The chief ramification of the enhanced EIA was strong GPS scintillation which was observed poleward of 30° northern MLAT and lasted until 8:00 local time. In total, the scintillation lasted for ~5 hours at latitudes north of 20° MLAT in central America.

## Plain Language Summary

Low latitude ionosphere is conducive to a Rayleigh-Taylor instability inherent to the region where magnetic field lines are parallel to the Earth. The instability's growth rate typically peaks just after sunset, whereby an enhanced eastward electric field at the terminator facilitates its growth. The instability promotes profound density depletions to rise into higher altitudes, where small scale irregularities develop. The resulting density irregularities are the most profound space weather threat to traversing radio signals. The timing of the scintillating signals follows the development of the instability, thereby the post-sunset local times are the most susceptible to radio scintillations. We present observations where this instability developed in the early morning, and rapidly expanded at the sunrise instead. The instabilities caused severe scintillations of GPS signals, reaching latitudes of Yucatan, Mexico.

## 1 Introduction

Convective ionospheric storms (CIS) in the low-latitude ionosphere have been and continue to be a subject of intense theoretical and experimental studies. The CIS (Woodman & La Hoz, 1976; Ossakow & Chaturvedi, 1978; Hysell, 2000; Kelley et al., 2011) destabilizes ionospheric plasma near the magnetic equator by virtue of the Rayleigh-Taylor Instability (RTI). The instability facilitates the rise of plasma depletions (Equatorial Plasma bubbles, or EPB) that reach the topside ionosphere and advect down along the field lines to the low-latitude ionosphere, stretching between the EIA peaks (Hysell, 2000; Groves et al., 1997). The EPBs consist of a large spatial spread of underlying density irregularities (Ossakow, 1981; Kelley et al., 2011, cf.), which profoundly affect traversing radio-waves by means of Fresnel diffraction off the irregularities at scales around  $\sqrt{2\lambda Z}$  ( $\lambda$  being signal's wavelength, and  $Z$  distance from a receiver) (Kintner et al., 2007), that is about 400 m at the GPS frequencies.

A consequence of the Fresnel diffraction is a scintillating signal's amplitude (Yeh & Liu, 1982; Basu et al., 1988; Groves et al., 1997), with a peculiar local time distribution which normally emerges after sunset, sometimes extending into the post-midnight sector (Basu et al., 1988; Béniguel et al., 2009; de Oliveira Moraes et al., 2017; Béniguel, 2019). The destabilizing driver that fosters the growth rate of the RTI and hence scintillation is the eastward electric field at the equator. The field normally peaks after sunset – the pre-reversal enhancement (Farley et al., 1986) – whose strength is modulated by geomagnetic activity and seasonality (Fejer & Scherliess, 1997).

Sporadic observations and reports of EPB near pre-sunrise local times have been reported (Burke, 1979; Fukao et al., 2003; de La Beaujardière et al., 2009; Zakharenkova et al., 2015; Wu et al., 2020); however, not much attention was given to these events, and our understanding of the impact on low-latitude TEC and scintillation is limited. A review of post-midnight EPBs points out that they preferentially occur during the geomagnetically quiet summer months of low solar activity (Otsuka, 2018). Nominal statistics

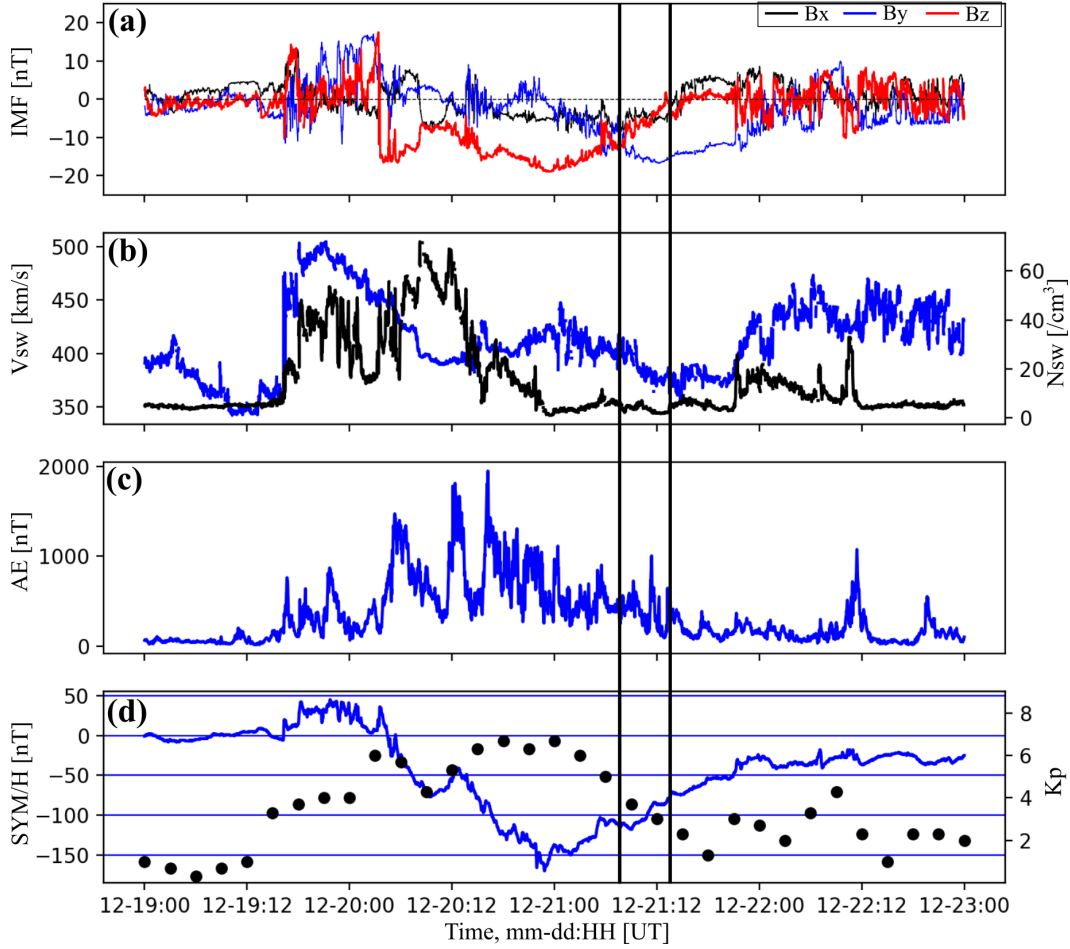


**Figure 1.** Solar wind and geomagnetic indices from the OMNIweb database. The time period under investigation is marked with vertical black lines. (a) Interplanetary magnetic field; (b) Solar wind speed (blue) and density (black). (c) Auroral electrojet index. (d) Sym/H (blue) and Kp (black) indices.

of radio (primarily GPS) amplitude scintillations (Basu et al., 1988; Béniguel et al., 2009; Jiao & Morton, 2015; de Oliveira Moraes et al., 2017) do not capture these events due to low frequency. Furthermore, the pre-sunrise EPBs normally cannot scintillate the GPS signals due to low plasma density at this local time (e.g., Otsuka, 2018). On the other hand, some case studies (Fukao et al., 2003; Zakharenkova et al., 2015; Wu et al., 2020) show dawn-time EPBs during winter months and geomagnetically disturbed days, just like the event we analyze in the remainder of this report. We present observations of the pre-dawn EPBs within the unusually episodic increase in EIA. In turn, the event caused severe GPS scintillations lasting for >5 hours and expanding poleward of 30°MLAT. We show how the EPBs evolved in space and time, and how they affected the signals of high-rate geodetic in Central America and the Caribbean using instantaneous scintillation maps (cf. Mrak et al., 2020).

## 2 Observations

The GPS scintillation event occurred during a geomagnetically active period, as depicted in Figure 1. A high-speed solar wind with a northward oriented interplanetary magnetic field (IMF) hit the magnetopause on 19 December 2015. The IMF turned southward on the next day, fueling a geomagnetic storm intensification indicated by negative deflection in the SYM/H index. The storm reached its peak with SYM/H  $\approx$  -150 nT and the Planetary K index (Kp) reaching 7<sup>-</sup> (numerical 6.7). The storm main phase was accompanied by several intense substorm injections indicated by the Auroral Electrojet (AE) index spikes exceeding 1000 nT. The IMF remained southward for about 30 hours. The scintillation event was observed in the American longitude sector, and it occurred in the storm recovery phase (increasing SYM/H), indicated by the time period between the two vertical lines.

We utilize 1-second UNAVCO GPS receivers located in Central America and the Caribbeans as scintillation monitors. We use computed scintillation indices to produce 2D maps of scintillation occurrence and strength. Due to the hardware limitations, we use Total Electron Content (TEC) to derive phase scintillation index  $\sigma_{TEC}$  (Beach & Kintner, 1999; Mrak et al., 2020), and amplitude scintillation index  $SNR_4$  derived from signal-to-noise ratio (SNR). While the former is defined as the usual phase scintillation index using standard deviation over 1 minute, the latter is computed in the same manner. The conventional normalization by mean intensity is avoided for the reasons discussed by Mrak et al. (2020) in great detail.

$$\sigma_{TEC} = \sqrt{\langle \delta TEC^2 \rangle - \langle \delta TEC \rangle^2} \quad (1)$$

$$SNR_4 = \sqrt{\langle \delta SNR^2 \rangle - \langle \delta SNR \rangle^2} \quad (2)$$

here,  $\langle \cdot \rangle$  is a temporal average operation, and  $\delta$  denotes a high-pass filtered quantity with a cut-off frequency of 0.1 Hz. The line-of-sight  $SNR_4$  scintillation index was converted to vertical via mapping function upon calculation (Spogli et al., 2009). We use a receiver dependent threshold for scintillation indices, thereby only values with 2.5 times above the receiver noise floor are used (cf. Mrak et al., 2020). We use the traditional scintillation index  $S_4$  on a single receiver to demonstrate the scintillation intensity. Totally 38 receivers were available during the storm period, with spatial distribution depicted by the magenta markers in Figure 2a. We utilize available spatial distribution of the receivers and construct scintillation maps in Figure 2 using the method described by (Mrak et al., 2020). The underlying TEC maps were obtained from the MIT Haystack GPS-TEC data product (Vierinen et al., 2016).

We present a sequence of the scintillation maps starting around sunrise in Figure 2. The cyan solid line in the maps denotes the local sunrise terminator at 350 km altitude. A broken cyan line is a magnetic conjugate location of the sunrise terminator mapped from the southern hemisphere, hereafter referred to as the conjugate sunrise terminator. We refer to the conjugate sunlit as a region between the conjugate sunrise terminator and local sunrise terminator in the northern hemisphere as marked in Figure 2b. The scintillation maps include locations and median values of amplitude scintillation index (red dots) recorded within 15 minutes before the panel's epoch. Scintillation indicators are overlaid on top of TEC maps. The elongated region of elevated TEC is the northern crest of EIA, lingering over central America just south of the 20°MLAT parallel. The EIA shows characteristic interhemispheric asymmetry, whereby the northern crest (winter hemisphere) was more abundant compared to the southern crest. This feature is climatological, due to increased O/N<sub>2</sub> ratio in the winter hemisphere, and meridional winds blowing from summer-to-winter hemisphere (Huang et al., 2018). The southernmost GPS receivers were located near 20°MLAT. These receivers measured first scintillating signals with the traversing conjugate sunrise terminator (Figure 2b). The scintillation area remained within the EIA, fixed in geographic location, for a duration of the conjugate sunlit (panels b – d). The scintillation then rapidly expanded poleward

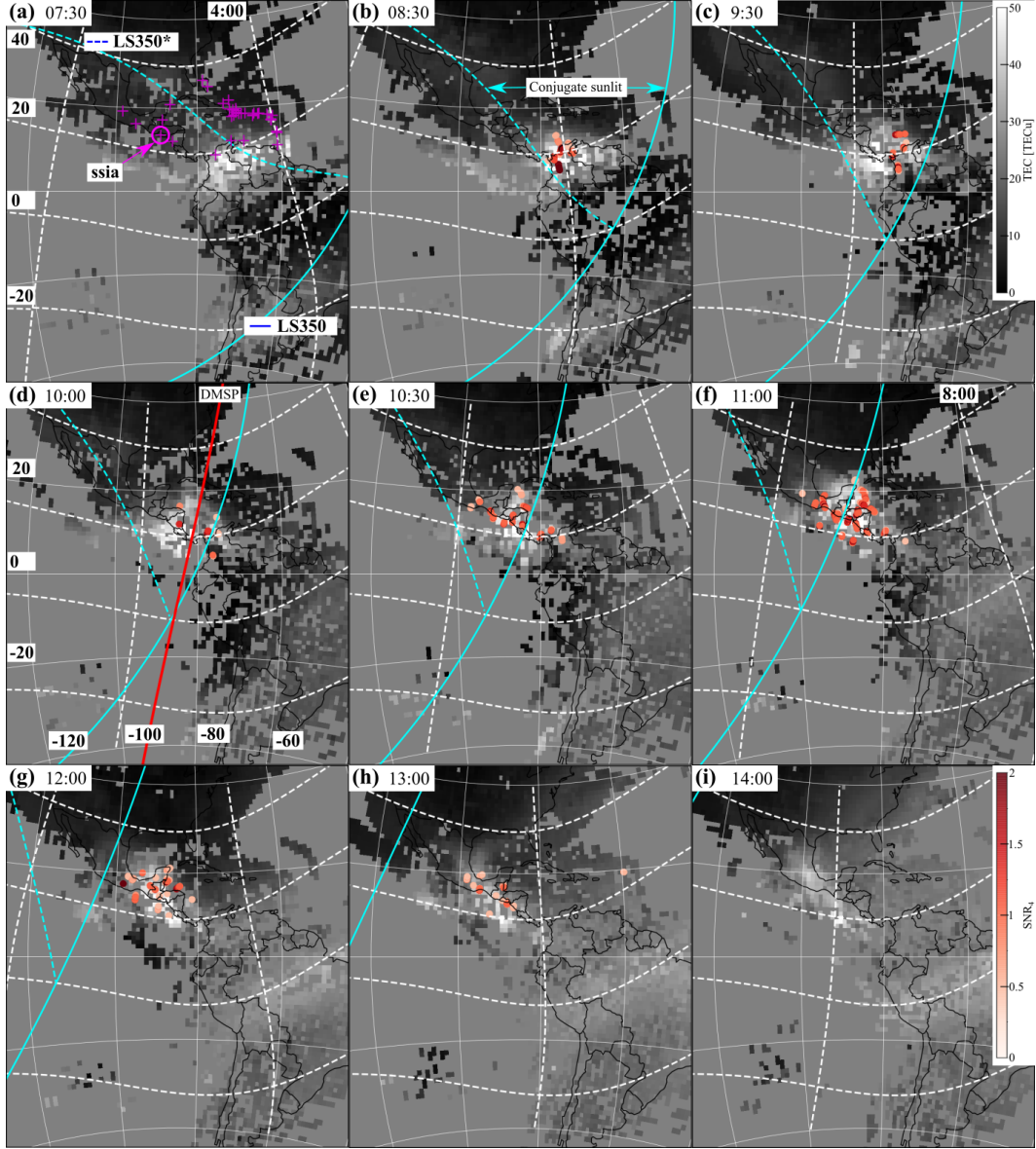


**Figure 2.** (a–i) Scintillation maps depicting location and strength of amplitude scintillation index  $SNR_4$  as red dots. The solid cyan line is the local sunrise terminator at 350 km altitude, and the dashed blue line is the conjugate sunrise terminator (see text for details). Panel (a) depicts locations of the 1-Hz GPS receivers (magenta markers). Panel (c) includes red line fiducial, representing the DMSP F16 trajectory. (g) Receivers’ averaged and normalized time-series presentation of amplitude (red) and phase (black) scintillation (see text for details). Continuous lines are for the event, whereas markers denote scintillation measured on 18th December 2015.

and westward at the time of the local sunrise terminator. The scintillation regions were tightly coupled to the expansion of the underlying EIA. The scintillation then slowly decayed as TEC decreased in two hours after the local sunrise. A video with a 5-minute resolution is available as supplemental material (Movie S1).

Total scintillation occurrence and strength as a function of Universal Time (UT), and Magnetic Local Time (MLT) is presented in Figure 3. We plot lines-of-sight-averaged

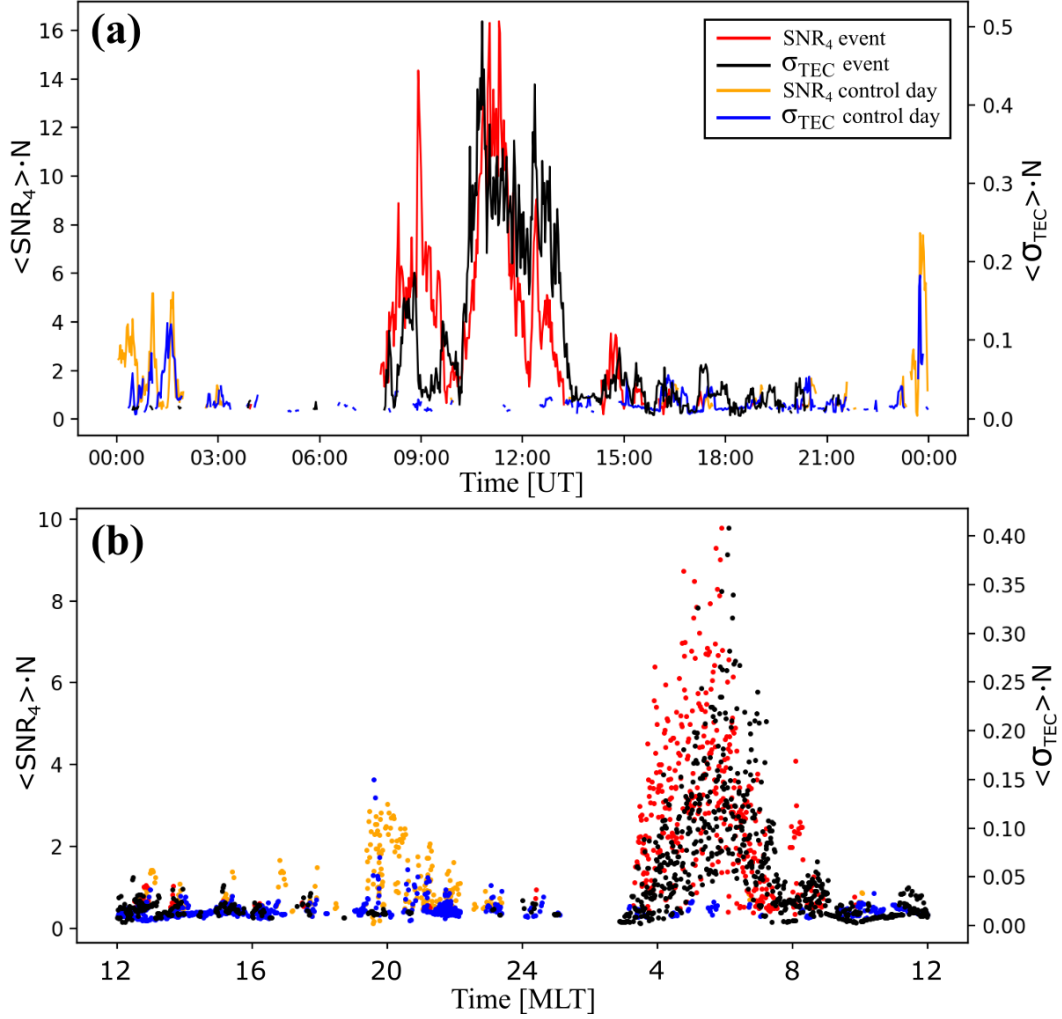


**Figure 3.** Time-series plots of median scintillation index receiver-averaged and normalized time-series presentation of amplitude (red) and phase (black) scintillation (see text for details). Continuous lines are for the event, whereas markers denote scintillation measured on 18th December 2015.

scintillation indices ( $\langle \cdot \rangle$ ), multiplied by the total number of recorded scintillation events  $N$  at any given time. Two distinct scintillation intensifications stand out as a function of UT, per the scintillation maps. The first peak corresponds to a period of conjugate sunrise, whereas the second intensification took off with the local sunrise. The area over central America was affected by this exceptional space weather phenomenon for a total of  $\sim 5$  hours. The bottom panel shows scintillation indices as a function of MLT, whereby locations of ionospheric piercing points were converted to geomagnetic coordinates. The scintillation emerged right before 4 MLT and decayed away by 9 MLT.

We compare this event with a control day which was chosen to be the most geomagnetically quiet day before this storm – 18th December 2015. This control day shows the usual scintillation occurrence, beginning near 19 MLT. On the other hand, no scintillation was measured in the pre-dawn sector. Scintillation occurrence on the control day follows the climatology pattern from south America (i.e., de Oliveira Moraes et al.,



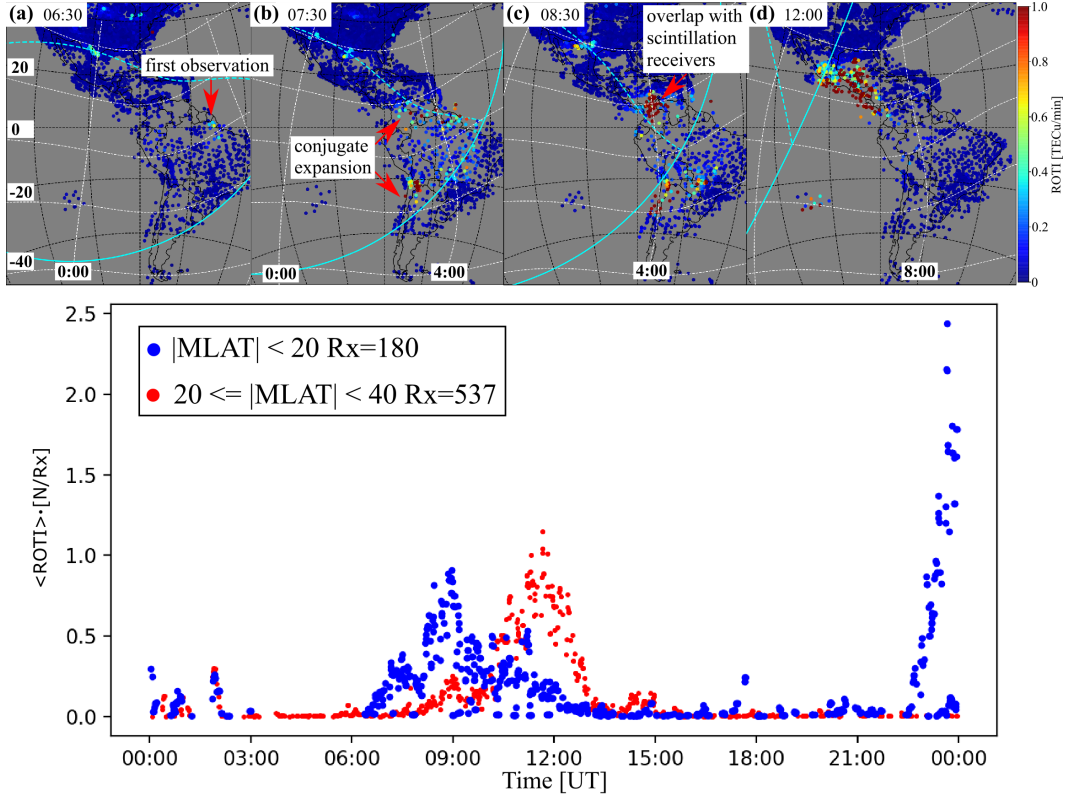


**Figure 4.** Development of ionospheric irregularities over the central and southern Americas using ROTI measurements. Top panel (a–d) ROTI maps at four time epochs depicting emergence of the EPBs, and their expansion. Sunrise terminators are the same as in Figure 2. Bottom panel shows time-series plots of ROTI occurrence in two latitude bands: (blue)  $|\text{MLAT}| < 20^\circ$ , and  $20^\circ < |\text{MLAT}| < 40^\circ$ . Unit normalization is explained in the text.

2017). There is a distinct time shift between the two days, which pictorially bolsters anomalous scintillation timing recorded on the 21st December 2015.

A more detailed look into the development of the EPBs is presented in Figure 4, where we utilize the line-of-sight TEC data used to produce the TEC maps in Figure 2. Here, the measure of irregularities is Rate of TEC change Index (ROTI) (cf. Pi et al., 1997). The important snapshots depicting the timing and expansion of the EPBs are presented in the top row. First signatures of the EPBs were observed at 6:30 UT (3:30 LT) near the magnetic equator just south of French Guyana. The EPBs expanded westward (and earlier in local time to  $\sim 3$  LT) and poleward, showing characteristic conjugacy. Scintillation in the southern hemisphere was not measured directly, but based on comparable ROTI values we assume the GPS scintillation was present there, though more subtle due to lower background TEC. The irregularities reached  $20^\circ$  MLAT, the equatorward edge of the high-rate receivers, at 8:30 UT – the time of the scintillation onset measured by the scintillation receivers (e.g., Figure 2).

The universal-time series of ROTI occurrence, for  $\text{ROTI} > 0.5$  TECu/min, is depicted in the bottom panel of Figure 4. The occurrence is split into two latitudinal segments, the band below with  $|\text{MLAT}| < 20^\circ$  and bands of  $20^\circ < |\text{MLAT}| \leq 40^\circ$ . The units of ROTI occurrence are computed as a median value of ROTI ( $\langle \text{ROTI} \rangle$ ) multiplied by the number of instances  $N$  and normalized by number of receivers  $Rx$  in the



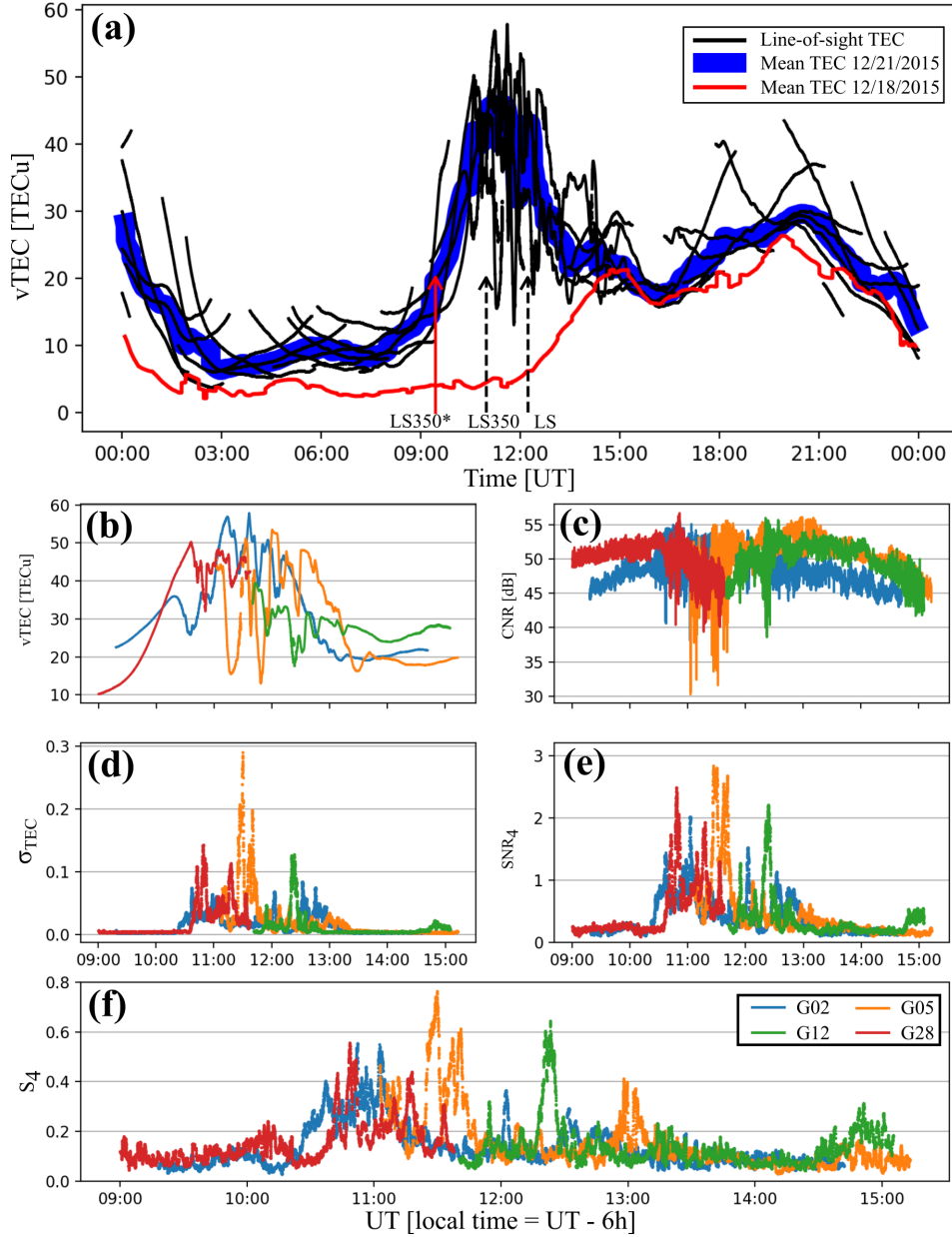


**Figure 5.** Data derived from SSIA receiver located in Honduras. (a) Vertical TEC on the day of the event for individual GPS satellites above 30 deg elevation (black), the blue line is averaged vTEC, and the red line is averaged vTEC on 18th December 2015. Markers denote sunrises (description in text). (b–e) Parameter estimates for four GPS satellites: (b) vTEC, (c) carrier-to-noise ratio CNR, (d) phase scintillation index  $\sigma_{TEC}$ , (e) amplitude scintillation index  $SNR_4$ . (f) Conventional amplitude scintillation index  $S_4$  for reference.

segment. The blue dots depict the region of EPBs closer to the equator, beyond the field-of-view (FOV) of the scintillation receivers. The red dots represent latitudes with FOV overlapping the scintillation receivers. The latter plot follows the trend-line of the scintillation in Figure 3a with the first increase near 9:00 UT, and the subsequent maxima just before 12:00 UT. The full development of low-latitude irregularities captured by ROTI maps is available in the supplemental movie S2.

We examine this phenomenon from a single receiver (SSIA, Honduras 89.12°W, 13.7°N) point-of-view, located underneath the scintillation region in the northern hemisphere. We plot vertical TEC (vTEC) from this receiver over the day in Figure 5a. We convert slant TEC to vTEC via differential receiver bias estimation based on the minimization of standard deviation (Ma & Maruyama, 2003). The thick blue line is average vTEC over lines-of-sight above 30-degree elevation angle. For comparison, averaged vTEC measured on 18th December (the control day) is plotted as the red line. Local sunrise times are marked for the receiver location. The TEC enhancement began at the time of conjugate sunrise (LS350\*), with a total TEC increase from  $\sim 10$  to  $\sim 50$  TECu (TECu,  $1 \text{ TECu} = 10^{16}$  electrons per square meter). Large perturbations in the vTEC started developing before a local sunrise terminator at 350 km (LS350). The perturbations decayed away together with decreasing background TEC starting at the local sunrise at the ground (LS). Remarkably, the total TEC reached a daily peak at the sunrise, exceeding a normal daily daytime peak with TEC below 30 TECu.

We show the four most affected lines-of-sight in panels b–f in Figure 5. TEC depletions within the anomalous enhancement exceeded 30 TECu. They had embedded smaller perturbations with noticeable data gaps marking losses of signal. In panel (c), huge variations in CNR are co-linear with the TEC depletions, whereby signal fading exceeded 10 dB. In the next row (d–e), the derived scintillation indices are presented, and in the bottom, the nominal scintillation index  $S_4$  is presented as a reference. The  $S_4$  was computed from the CNR, converted to intensity  $I = 10^{\text{CNR}/10}$ , and calculated as  $S_4^2 = \sigma_I / \langle I \rangle$  (i.e., Rodrigues & Moraes, 2019).

Lastly, the Defense Meteorological Space Program (DMSP) F16 traversed the anomalous density region in central America near 10 UT, with its trajectory drawn in Figure 2d. *In-situ* ion density, perpendicular ion flow components, and plasma temperatures are presented in Figure 6. This southbound pass encountered a sharp density gradient near 30°MLAT, with a total increase of about an order of magnitude. This occurred in the region where the GPS receivers measured the large TEC enhancement at dawn, reaching  $\sim 50$  TECu. Right within the region of enhanced plasma, plasma irregularities resided in the topside ionosphere ( $\sim 850$  km), identified with a high-pass filtered (0.1 Hz) ion density (dNi) in the second panel. Another set of plasma irregularities embedded within density depletions were measured adjacent to the magnetic equator. Both irregularity regions were accompanied with subtle increase in ion and electron temperatures. Additionally, ion flow perturbations near the equator are positively correlated with the density irregularities, with a net eastward (sunward) horizontal flow ( $v_H$ ), and upward flow ( $v_Z$ ) of  $> 100$  m/s at the equator. The DMSP did not measure density irregularities in the southern hemisphere at a local time 20 minutes earlier than in the northern hemisphere.

### 3 Discussion

Sporadic observations of storm-time EPBs near sunrise have been reported (e.g., Fukao et al., 2003; Zakharenkova et al., 2015; Wu et al., 2020), but appear to be a rare phenomenon which does not cause (measurable) scintillations at GPS frequencies due to low background density. The RTI is unstable in a presence of upflow (eastward electric field) at the magnetic equator (Hysell, 2000; Martinis et al., 2005); however, normal condition at dawn is westward electric field (Fejer & Scherliess, 1997), hence a zonal reversal is necessary for the RTI to operate. It has been shown that such reversals do occur at geomagnetically disturbed periods (Fejer et al., 1976; Bowman, 1978). Additionally, it has been speculated that in these kinds of circumstances, RTI could be operating together with the  $\mathbf{E} \times \mathbf{B}$  instability (Burke, 1979). Long-lasting auroral activity drives the disturbance dynamo, which nudges the RTI with high efficiency in time delay below 12 hours, and between 20 to 30 hours (Scherliess & Fejer, 1997). Moreover, the disturbance dynamo effect peaks near 4:00 local time (Fejer et al., 1999). This is the local time we found onset of the EPBs (cf., Figure 4).

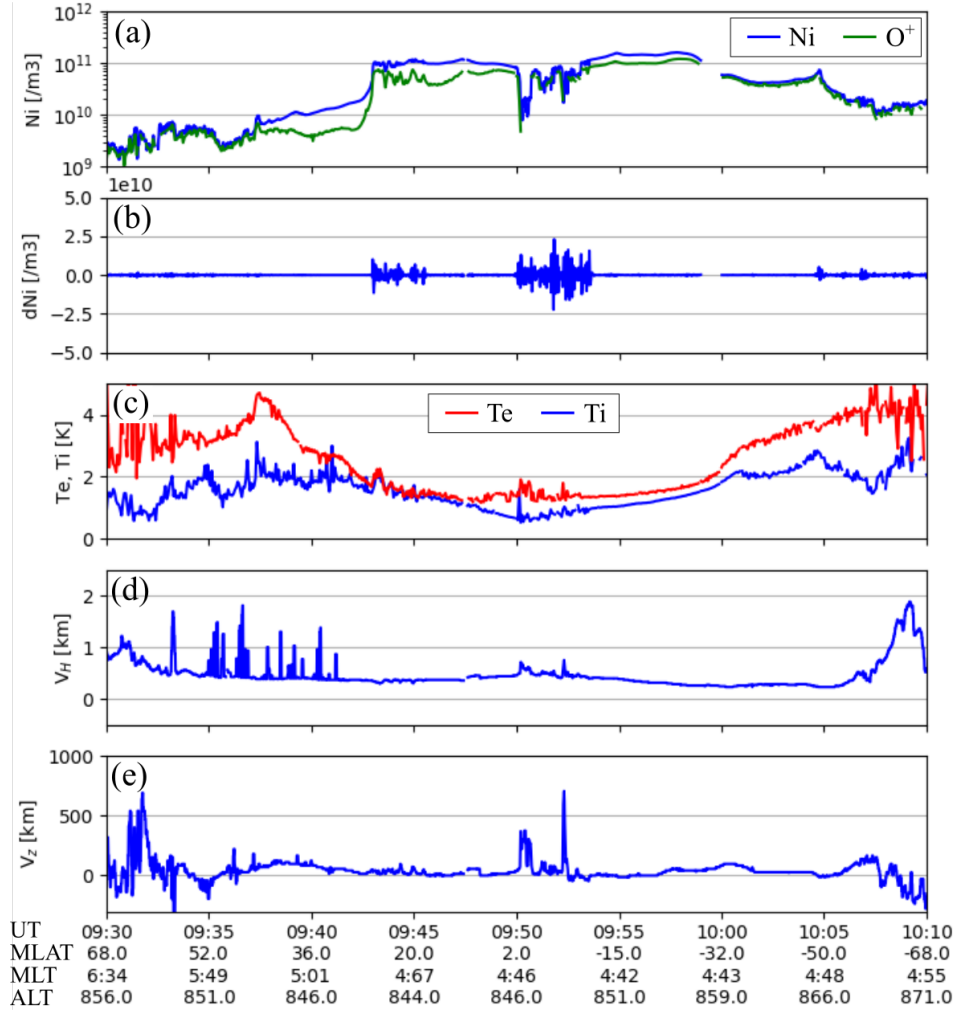


**Figure 6.** DMSP F16 measurements of plasma parameters during a recorded scintillation time period. (a) Ion density, (b) 0.1 Hz high-pass filtered ion density, (c) Electron (Te) and ion (Ti) temperatures, (d) horizontal (cross-track) ion drift (positive sunward), (e) vertical ion drift (positive up).

The presented event provides a new insight in terms of preconditioning, timing, and intensity of pre-dawn space weather at low-latitudes. We show that the EIA persisted throughout the night. Thus an uncharacteristically abundant plasma basin lingered in the pre-dawn equatorial ionosphere. The initial onset of the CIS accompanying an episodic TEC increase began at just before 6:30 UT, (4 MLT). A subtle decrease in IMF Bz occurred at that time, however, but there was no other abrupt changes in the solar wind or geomagnetic indices. Both, the timing and the absence of geomagnetic disturbances reinforce the disturbance dynamo as the most likely driver of these pre-dawn EPBs. Similarly, the disturbance dynamo was discussed as the most likely driver for pre-dawn density depletions observed by the Communication/Navigation Outage Forecasting System (C/NOFS) satellite (Su et al., 2009; de La Beaujardière et al., 2009). The only macroscopic driver that could bolster the intensity of the disturbance dynamo effect was longevity ( $\sim 30$  hours) of the southward IMF, and hence auroral activity, prior to the EPBs onset.

Observation of storm-time pre-dawn EPBs observed by Swarm satellites was examined in detail for 14 February 2014 storm (Zakharenkova et al., 2015). While the geomagnetic conditions and the geolocation were very similar to the event presented in this report, we did not find any ground-based GPS scintillations during that storm. They utilized TIE-GCM to model the disturbance dynamo, very similar to the observed peak by C/NOFS in the pre-dawn sector (de La Beaujardière et al., 2009). The seasonality of these EPBs is particularly intriguing considering the efficiency of the RTI decreases with increasing asymmetry between conjugate E-region conductance (Martinis et al., 2005). The irregularities measured by GPS scintillation and ROTI expanded most significantly at about 10:00 UT near the western coast of South America. There, the angle between the sunrise terminator and magnetic declination is the biggest, hence the RTI efficiency is the lowest. Therefore, the disturbance dynamo was likely enhanced by a secondary source of the eastward electric field. One such candidate would be a penetration of overshielding electric field due to substorm activity at high-latitudes. The auroral electrojet remained active with  $AE \sim 500$  nT. Overshielding at these local times shall enhance equatorial electrojet (e.g., Ebihara et al., 2014), however, the occurrence of such events is very low (Hashimoto et al., 2017).

The EIA density and scintillation significantly increased with an approach of the sunrise, expanding beyond  $35^\circ$ MLAT. The scintillation increase was accompanied by further TEC enhancement was facilitated by photo-ionization, elevating the TEC to  $\sim 50$  TECu. The sudden poleward expansion was a manifestation of continuous upwelling at the equator, whereby the EPBs must have had expanded to beyond 3,500 km in the equatorial plane in order to map to  $35^\circ$ MLAT. While a climatological model for the equatorial electric field during geomagnetically disturbed times has a westward-to-eastward reversal just before 4 MLT (Fejer & Scherliess, 1997), the resulting upwelling shall be subtle with vertical velocity  $< 40$  m/s (e.g., Fejer & Scherliess, 1997; Su et al., 2009; Zakharenkova et al., 2015). In aggregate, pre-dawn EPBs by themselves are rather climatological, however, the extent of EIA expansion, TEC increase, and accompanying GPS scintillations were unprecedented. For reference, a preliminary survey for pre-dawn GPS scintillations using the same dataset (Mrak et al., 2020) in the years 2012 – 2019 revealed that this particular storm was the only such event in the American longitude sector.

## 4 Summary

We presented an episodic expansion of the EIA, increase in TEC, and GPS scintillation near dawn (3:30 MLT – 9:00 MLT) in the American longitude sector ( $110^\circ$ W –  $30^\circ$ W). The observations show that the EIA had persisted throughout the night, and became a region of scintillation-producing plasma irregularities. The EIA density abruptly elevated to  $\sim 50$  TECu at dawn, exceeding the nominal afternoon TEC peak by almost a factor of two. Scintillation intensity followed the TEC trend. Large-scale analysis using ROTI measurements shows the irregularities emerged earlier at 6:30 UT (3:30 MLT in Brazil) near the magnetic equator. The irregularities reached  $20^\circ$ MLAT, that is the equatorward edge of the scintillation receivers, two hours after their onset. Then, the irregularities expanded poleward beyond  $35^\circ$ MLAT at local sunrise in the northern hemisphere.

Climatological models do not capture the pre-dawn EPBs, neither do they predict GPS scintillations at these local times. The pre-dawn irregularities are much more nuanced, whereby only data assimilation model considering C/NOFS electric field measurements successfully reproduced EPBs at dawn (Su et al., 2009). Similarly, a thorough survey for pre-dawn irregularities and scintillations shall be conducted to better understand geomagnetic drivers, thereby improve the models to predict such severe space weather. In particular, pre-dawn space weather events causing severe GPS scintillations expanding beyond  $30^\circ$ MLAT pose a significant risk for trans-ionospheric radio disruptions.

## Acknowledgments

The study was supported by NSF-AGS 1821135, NSF-AGS-1907698, NASA-80NSSC18K0657, and AFOSR FA9559-16-1-0364 awards to Boston University. GPS TEC maps as well as DMSP data were retrieved from open madrigal database <http://cedar.openmadrigal.org/>. Solar wind and geomagnetic indices are available via <https://cdaweb.sci.gsfc.nasa.gov/pub/data/omni/>. High-rate data used to process scintillation indices is freely available from UNAVCO high-rate 1-Hz data repository found at <https://www.unavco.org/data/gps-gnss/ftp/ftp.html>.

## References

- Basu, S., MacKenzie, E., & Basu, S. (1988, may). Ionospheric constraints on VHF/UHF communications links during solar maximum and minimum periods. *Radio Science*, 23(3), 363–378. Retrieved from <http://doi.wiley.com/10.1029/RS023i003p00363> doi: 10.1029/RS023i003p00363
- Beach, T. L., & Kintner, P. M. (1999, oct). Simultaneous Global Positioning System observations of equatorial scintillations and total electron content fluctuations. *Journal of Geophysical Research: Space Physics*, 104(A10), 22553–22565. Retrieved from <http://doi.wiley.com/10.1029/1999JA900220> doi: 10.1029/1999JA900220
- Béniguel, Y. (2019). Ionospheric Scintillations: Indices and Modeling. *Radio Science*, 54(7), 618–632. doi: 10.1029/2018RS006655
- Béniguel, Y., Adam, J. P., Jakowski, N., Noack, T., Wilken, V., Valette, J. J., ... Arbesser-Rastburg, B. (2009). Analysis of scintillation recorded during the PRIS measurement campaign. *Radio Science*, 44(5), 1–11. doi: 10.1029/2008RS004090
- Bowman, G. (1978, jun). A relationship between polar magnetic substorms, ionospheric height rises and the occurrence of spread-F. *Journal of Atmospheric and Terrestrial Physics*, 40(6), 713–722. Retrieved from <https://linkinghub.elsevier.com/retrieve/pii/0021916978901290> doi: 10.1016/0021-9169(78)90129-0
- Burke, W. I. (1979). Plasma bubbles near the dawn terminator in the topside ionosphere. *Planetary and Space Science*, 27(9), 1187–1193. doi: 10.1016/0032-0633(79)90138-7
- de La Beaujardière, O., Retterer, J. M., Pfaff, R. F., Roddy, P. A., Roth, C., Burke, W. J., ... Cooke, D. L. (2009, aug). C/NOFS observations of deep plasma depletions at dawn. *Geophysical Research Letters*, 36(18), L00C06. Retrieved from <http://doi.wiley.com/10.1029/2009GL038884> doi: 10.1029/2009GL038884
- de Oliveira Moraes, A., Costa, E., Abdu, M. A., Rodrigues, F. S., de Paula, E. R., Oliveira, K., & Perrella, W. J. (2017). The variability of low-latitude ionospheric amplitude and phase scintillation detected by a triple-frequency GPS receiver. *Radio Science*, 52(4), 439–460. doi: 10.1002/2016RS006165
- Ebihara, Y., Tanaka, T., & Kikuchi, T. (2014, sep). Counter equatorial electrojet and overshielding after substorm onset: Global MHD simulation study. *Journal of Geophysical Research: Space Physics*, 119(9), 7281–7296. Retrieved from <http://doi.wiley.com/10.1002/2014JA020065> doi: 10.1002/2014JA020065
- Farley, D. T., Bonelli, E., Fejer, B. G., & Larsen, M. F. (1986). The prereversal enhancement of the zonal electric field in the equatorial ionosphere. *Journal of Geophysical Research*, 91(A12), 13723. Retrieved from <http://doi.wiley.com/10.1029/JA091iA12p13723> doi: 10.1029/JA091iA12p13723
- Fejer, B. G., Farley, D. T., Balsley, B. B., & Woodman, R. F. (1976, sep). Radar studies of anomalous velocity reversals in the equatorial ionosphere. *Journal of Geophysical Research*, 81(25), 4621–4626. Retrieved from <http://doi.wiley.com/10.1029/JA081i025p04621> doi: 10.1029/JA081i025p04621



- Fejer, B. G., & Scherliess, L. (1997, nov). Empirical models of storm time equatorial zonal electric fields. *Journal of Geophysical Research: Space Physics*, 102, 24047–24056. Retrieved from <http://doi.wiley.com/10.1029/97JA02164> doi: 10.1029/97JA02164
- Fejer, B. G., Scherliess, L., & de Paula, E. R. (1999, sep). Effects of the vertical plasma drift velocity on the generation and evolution of equatorial spread F. *Journal of Geophysical Research: Space Physics*, 104(A9), 19859–19869. Retrieved from <http://doi.wiley.com/10.1029/1999JA900271> doi: 10.1029/1999JA900271
- Fukao, S., Ozawa, Y., Yamamoto, M., & Tsunoda, R. T. (2003, nov). Altitude-extended equatorial spread F observed near sunrise terminator over Indonesia. *Geophysical Research Letters*, 30(22), 3–6. Retrieved from <http://doi.wiley.com/10.1029/2003GL018383> doi: 10.1029/2003GL018383
- Groves, K. M., Basu, S., Weber, E. J., Smitham, M., Kuenzler, H., Valladares, C. E., ... Kendra, M. J. (1997, sep). Equatorial scintillation and systems support. *Radio Science*, 32(5), 2047–2064. Retrieved from <http://doi.wiley.com/10.1029/97RS00836> doi: 10.1029/97RS00836
- Hashimoto, K. K., Kikuchi, T., Tomizawa, I., & Nagatsuma, T. (2017). Substorm Overshielding Electric Field at Low Latitude on the Nightside as Observed by the HF Doppler Sounder and Magnetometers. *Journal of Geophysical Research: Space Physics*, 122(10), 10,851–10,863. doi: 10.1002/2017JA024329
- Huang, H., Lu, X., Liu, L., Wang, W., & Li, Q. (2018, dec). Transition of Interhemispheric Asymmetry of Equatorial Ionization Anomaly During Solstices. *Journal of Geophysical Research: Space Physics*, 123(12), 2018JA026055. Retrieved from <https://onlinelibrary.wiley.com/doi/abs/10.1029/2018JA026055> doi: 10.1029/2018JA026055
- Hysell, D. (2000, aug). An overview and synthesis of plasma irregularities in equatorial spread F. *Journal of Atmospheric and Solar-Terrestrial Physics*, 62(12), 1037–1056. Retrieved from <https://linkinghub.elsevier.com/retrieve/pii/S136468260000095X> doi: 10.1016/S1364-6826(00)00095-X
- Jiao, Y., & Morton, Y. T. (2015, sep). Comparison of the effect of high-latitude and equatorial ionospheric scintillation on GPS signals during the maximum of solar cycle 24. *Radio Science*, 50(9), 886–903. Retrieved from <https://onlinelibrary.wiley.com/doi/abs/10.1002/2015RS005719> doi: 10.1002/2015RS005719
- Kelley, M. C., Makela, J. J., de La Beaujardière, O., & Retterer, J. (2011, jun). Convective Ionospheric Storms: A Review. *Reviews of Geophysics*, 49(2), RG2003. Retrieved from <http://doi.wiley.com/10.1029/2010RG000340> doi: 10.1029/2010RG000340
- Kintner, P. M., Ledvina, B. M., & de Paula, E. R. (2007, sep). GPS and ionospheric scintillations. *Space Weather*, 5(9). Retrieved from <http://doi.wiley.com/10.1029/2006SW000260><http://files/178/rds1552.pdf><http://files/248/rds1992.pdf><http://files/247/swe177.pdf> doi: 10.1029/2006SW000260
- Ma, G., & Maruyama, T. (2003). Derivation of TEC and estimation of instrumental biases from GEONET in Japan. *Annales Geophysicae*, 21(10), 2083–2093. Retrieved from [www.ann-geophys.net/21/2083/2003/angeo-21-2083-2003](http://www.ann-geophys.net/21/2083/2003/angeo-21-2083-2003)<http://www.ann-geophys.net/21/2083/2003/> doi: 10.5194/angeo-21-2083-2003
- Martinis, C. R., Mendillo, M., & Aarons, J. (2005). Toward a synthesis of equatorial spread F onset and suppression during geomagnetic storms. *Journal of Geophysical Research*, 110(A7), A07306. Retrieved from <http://doi.wiley.com/10.1029/2003JA010362> doi: 10.1029/2003JA010362
- Mrak, S., Semeter, J., Nishimura, Y., Rodrigues, F. S., Coster, A. J., & Groves, K. (2020, nov). Leveraging Geodetic GPS Receivers for Ionospheric Scintillation Science. *Radio Science*, 55(11). Retrieved from <https://onlinelibrary>

- .wiley.com/doi/10.1029/2020RS007131 doi: 10.1029/2020RS007131
- Ossakow, S. L. (1981, may). Spread-F theories—a review. *Journal of Atmospheric and Terrestrial Physics*, 43(5-6), 437–452. Retrieved from <https://linkinghub.elsevier.com/retrieve/pii/0021916981901070> doi: 10.1016/0021-9169(81)90107-0
- Ossakow, S. L., & Chaturvedi, P. K. (1978). Morphological studies of rising equatorial spread F bubbles. *Journal of Geophysical Research*, 83(A5), 2085. Retrieved from <http://doi.wiley.com/10.1029/JA083iA05p02085> doi: 10.1029/JA083iA05p02085
- Otsuka, Y. (2018, dec). Review of the generation mechanisms of post-midnight irregularities in the equatorial and low-latitude ionosphere. *Progress in Earth and Planetary Science*, 5(1), 57. Retrieved from <https://progearthplanetsci.springeropen.com/articles/10.1186/s40645-018-0212-7> doi: 10.1186/s40645-018-0212-7
- Pi, X., Mannucci, A. J., Lindqwister, U. J., & Ho, C. M. (1997, sep). Monitoring of global ionospheric irregularities using the Worldwide GPS Network. *Geophysical Research Letters*, 24(18), 2283–2286. doi: 10.1029/97GL02273
- Rodrigues, F. S., & Moraes, A. O. (2019). ScintPi: A Low-Cost, Easy-to-Build GPS Ionospheric Scintillation Monitor for DASI Studies of Space Weather, Education, and Citizen Science Initiatives. *Earth and Space Science*, 6(8), 1547–1560. doi: 10.1029/2019EA000588
- Scherliess, L., & Fejer, B. G. (1997, nov). Storm time dependence of equatorial disturbance dynamo zonal electric fields. *Journal of Geophysical Research: Space Physics*, 102(A11), 24037–24046. Retrieved from <http://doi.wiley.com/10.1029/97JA02165> doi: 10.1029/97JA02165
- Spogli, L., Alfonsi, L., De Franceschi, G., Romano, V., Aquino, M. H. O., & Dodson, A. (2009, sep). Climatology of GPS ionospheric scintillations over high and mid-latitude European regions. *Annales Geophysicae*, 27(9), 3429–3437. Retrieved from <https://www.ann-geophys.net/27/3429/2009/> doi: 10.5194/angeo-27-3429-2009
- Su, Y. J., Retterer, J. M., De La Beaujardière, O., Burke, W. J., Roddy, P. A., Pfaff, R. F., ... Hunton, D. E. (2009). Assimilative modeling of equatorial plasma depletions observed by C/NOFS. *Geophysical Research Letters*, 36(18), 2–5. doi: 10.1029/2009GL038946
- Vierinen, J., Coster, A. J., Rideout, W. C., Erickson, P. J., & Norberg, J. (2016). Statistical framework for estimating GNSS bias. *Atmospheric Measurement Techniques*, 9(3), 1303–1312. doi: 10.5194/amt-9-1303-2016
- Woodman, R. F., & La Hoz, C. (1976, nov). Radar observations of F region equatorial irregularities. *Journal of Geophysical Research*, 81(31), 5447–5466. Retrieved from <http://doi.wiley.com/10.1029/JA081i031p05447> doi: 10.1029/JA081i031p05447
- Wu, K., Xu, J., Yue, X., Xiong, C., Wang, W., Yuan, W., ... Luo, J. (2020). Equatorial plasma bubbles developing around sunrise observed by an all-sky imager and global navigation satellite system network during storm time. *Annales Geophysicae*, 38(1), 163–177. doi: 10.5194/angeo-38-163-2020
- Yeh, K. C., & Liu, C.-H. (1982). Radio wave scintillations in the ionosphere. *Proceedings of the IEEE*, 70(4), 324–360. Retrieved from <https://ieeexplore.ieee.org/document/1456581> doi: 10.1109/PROC.1982.12313
- Zakharenkova, I., Astafyeva, E., & Cherniak, I. (2015, oct). Early morning irregularities detected with spaceborne GPS measurements in the topside ionosphere: A multisatellite case study. *Journal of Geophysical Research: Space Physics*, 120(10), 8817–8834. Retrieved from <http://doi.wiley.com/10.1002/2015JA021447> doi: 10.1002/2015JA021447



# Supporting Information for Extreme low-latitude TEC enhancement and GPS Scintillation at dawn

Sebastijan Mrak<sup>1</sup>, Joshua Semeter<sup>1</sup>, Yukitoshi Nishimura<sup>1</sup>, and Anthea J.

Coster<sup>2</sup>

<sup>1</sup>Department of Electrical and Computer Engineering and Center for Space Physics, Boston University, Boston, MA, USA

<sup>2</sup>Haystack Observatory, Massachusetts Institute of Technology, Westford, MA, USA

## Additional Supporting Information (Files uploaded separately)

1. Captions for Movies S1

### Introduction

This file describes the attached Movie S1, which is an extension of Figure 2 or the main manuscript. Processing steps and organization is described in Section 2 of the main manuscript.

### Movie S1.

The Movie consists of a sequence of scintillation maps computed for 21st December 2015. The cyan solid line in the maps denotes the local sunrise terminator at 350 km altitude. The dashed blue line is a magnetic conjugate location of the sunrise terminator mapped from the southern hemisphere. The scintillation maps include locations and median values of amplitude scintillation index (red dots) recorded within 5 minutes prior

---

X - 2

:

to the panel's epoch. Location of the red dots was projected to 350 km altitude, the same altitude as the underlying TEC maps in grey scale.